A&A 606, A96 (2017)
DOI: 10.1051/0004-6361/201730819

Astronomy & Astrophysics

An X-ray/SDSS sample

II. AGN-driven outflowing gas plasma properties

M. Perna[1,2], G. Lanzuisi[1,3], M. Brusa[1,3], G. Cresci[2], and M. Mignoli[3]

[1] Dipartimento di Fisica e Astronomia, Università di Bologna, viale Berti Pichat 6/2, 40127 Bologna, Italy
e-mail: michele.perna4@unibo.it
[2] INAF–Osservatorio Astrofisico di Arcetri, Largo Enrico Fermi 5, 50125 Firenze, Italy
[3] INAF–Osservatorio Astronomico di Bologna, via Ranzani 1, 40127 Bologna, Italy

Received 19 March 2017 / Accepted 22 May 2017

ABSTRACT

Aims. Galaxy-scale outflows are currently observed in many active galactic nuclei (AGNs); however, characterisation of them in terms of their (multi-) phase nature, amount of flowing material, and effects on their host galaxy is still unresolved. In particular, ionised gas mass outflow rate and related energetics are still affected by many sources of uncertainty. In this respect, outflowing gas plasma conditions, being largely unknown, play a crucial role.
Methods. We have analysed stacked spectra and sub-samples of sources with high signal-to-noise temperature- and density-sensitive emission lines to derive the plasma properties of the outflowing ionised gas component. We did this by taking advantage of the spectroscopic analysis results we obtained while studying the X-ray/SDSS sample of 563 AGNs at $z < 0.8$ presented in our companion paper. For these sources, we also studied in detail various diagnostic diagrams to infer information about outflowing gas ionisation mechanisms.
Results. We derive, for the first time, median values for electron temperature and density of outflowing gas from medium-size samples (∼30 targets) and stacked spectra of AGNs. Evidence of shock excitation are found for outflowing gas.
Conclusions. We measure electron temperatures of the order of $\sim 1.7 \times 10^4$ K and densities of ~ 1200 cm^{-3} for faint and moderately luminous AGNs (intrinsic X-ray luminosity $40.5 < \log(L_X) < 44$ in the 2–10 keV band). We note that the electron density that is usually assumed ($N_e = 100$ cm^{-3}) in ejected material might result in relevant overestimates of flow mass rates and energetics and, as a consequence, of the effects of AGN-driven outflows on the host galaxy.

Key words. galaxies: active – quasars: emission lines – ISM: jets and outflows

1. Introduction

According to the most popular active galactic nuclei (AGN)-galaxy evolutionary models (e.g. Hopkins et al. 2008; Menci et al. 2008; Sijacki et al. 2015), the growth of a supermassive black hole (SMBH) has a significant impact on host galaxy evolution. The accompanying released accretion energy, coupling with the interstellar medium (ISM), has been postulated to regulate both the star formation processes in the host and the accretion onto the SMBH (e.g. King & Pounds 2015; Zubovas & King 2014).

The presence of AGN-driven outflows is nowadays quite well established through high resolution observations of local and high-redshift galaxies, and it is now possible to study in detail the feedback phenomena, characterising the galaxy-wide extension and the morphology of the ejected material as well as the masses and the energetics related to outflows (e.g. Bischetti et al. 2017; Brusa et al. 2016; Cresci et al. 2015; Feruglio et al. 2015; Harrison et al. 2012, 2014; Husemann et al. 2016; Perna et al. 2015a,b; Rupke & Veilleux 2013; see also Fiore et al. 2017, for an updated and complete list). However, the physical processes responsible for the coupling between AGN winds and the ISM remain largely unknown. Furthermore, outflow effects on host galaxy evolution, as derived from outflow energetics (mass outflow rate, kinetic and momentum powers), remain mostly unknown.

In Perna et al. (2017a; Paper I hereinafter) we presented a sample of 563 X-ray selected AGN at $z < 0.8$, for which SDSS spectra are available. We combined ionised emission line and neutral absorption feature information as modelled through multicomponent simultaneous fitting (Brusa et al. 2015), non-parametric measurement (Zakamska & Greene 2014), and a penalised pixel fitting procedure (pPXF; Cappellari & Emsellem 2004; Cappellari 2017) analysis, to derive kinematic properties of both warm and cold gas components of the ISM. The modelling of optical spectra allowed us to derive the incidence of ionised (∼40%) and atomic (<1%) outflows covering a wide range of AGN bolometric luminosity, from 10^{42} to 10^{46} erg/s and to relate the presence of ionised outflows with different AGN power tracers. We also derived X-ray and bolometric luminosities and we discuss our results in the context of an evolutionary sequence allowing for two distinct stages of the feedback phase: an initial stage characterised by X-ray and optical obscured AGNs in which the atomic gas is still present in the ISM and the outflow processes involve all the gas components, and a later stage associated with unobscured AGNs, which line of sight has been cleaned and the cold components have been heated or exhausted.

In this second paper we focus on the physical conditions of ionised gas, studying in details stacked spectra and small and medium-size sub-samples of X-ray/SDSS sources characterised by the presence of well detected optical diagnostic lines.

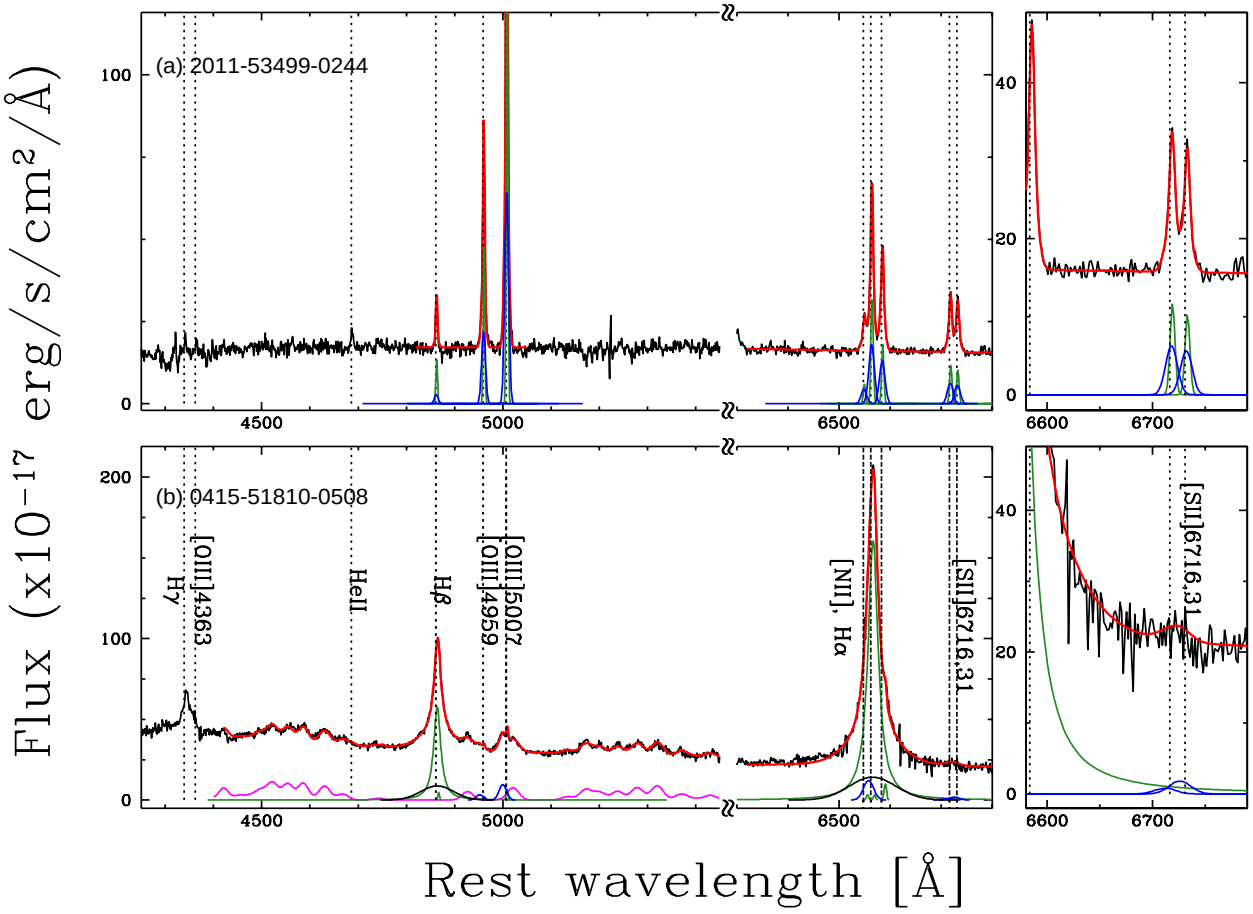

Fig. 1. Rest-frame optical spectra of two AGNs from our X-ray/SDSS sample. For each target, in *the upper left corner of the large panel* we show the MJD, the plate and the fibre numbers which uniquely identify the SDSS spectrum. The dashed vertical lines mark the location of the most prominent emission lines, besides some features crucial for the analysis presented in this paper and/or in Paper I. Fit results obtained in Paper I, from the multicomponent simultaneous fit in the Hβ-[O III] and Hα-[NII] regions are also shown: best-fit narrow component (NC) and broad line region component (BC) profiles are highlighted with green curves; outflow component (OC) and Fe II emission are shown with blue and magenta curves, respectively. Finally, black Gaussian profile in the *low panel* shows a second set of BC used to fit the complex BLR profiles (see Paper I for further details). The insets on the right of each panel show an enlargement of the sulphur lines. The spectra display faintness and blending problems affecting density-sensitive [S II]$\lambda\lambda$6716, 6731 and temperature-sensitive [O III]λ4363 emission lines. In particular, the object in the first panel displays a well detected and modelled sulphur doublet, from which we can easily derive the density-sensitive flux ratio, but faint oxygen λ4363 line; the spectrum in the *lower panel* shows blended sulphur doublet features and oxygen line at λ4363. For both the AGNs it is therefore not possible to derive temperature-sensitive flux ratios.

In particular, we focus on the estimate of the electron temperature (T_e) and density (N_e) of the unperturbed and outflowing ionised gas in the narrow line region (NLR).

Plasma properties of NLR unperturbed gas are now well constrained to average N_e of the order of ≈250–400 cm^{-3} and T_e of ∼1.5 × 10^4 K (e.g. Vaona et al. 2012; Zhang et al. 2013). The physical conditions within the outflowing regions are instead mostly unknown, because of the faintness of the outflow wings of the emission lines involved in the diagnostics used to derive such information (see e.g. De Robertis & Osterbrock 1986; Rice et al. 2006; Vaona et al. 2012). Knowledge of these properties is crucial for the investigation of the mechanisms responsible of outflows: it can significantly reduce the uncertainties in the outflow energetics (up to a factor of ten), improving our understanding of the AGN outflow phenomenon and its impact on galaxy evolution.

The paper is organised as follows. We first give a brief description of the spectroscopic modelling results obtained in Paper I (Sect. 2). In Sect. 3 we review the current knowledge of the NLR plasma conditions and its role in deriving the outflow energetics. In Sects. 3.2 and 3.1 we derive temperature- and density-sensitive flux ratios from single targets and stacked spectra. Section 3.3 displays the median plasma properties. In Sect. 4 we investigate several diagnostics to infer information about outflowing gas ionisation mechanisms. Finally, we summarise our results and their implications in the Discussion section (Sect. 5).

2. Previous work – optical spectroscopic analysis

In Paper I we presented modelling results for a sample of 563 AGNs. Thanks to multicomponent simultaneous fit technique, for each emission line in the wavelength range between He Iλ4687 and [S II]$\lambda\lambda$6716, 6731 doublet, we were able to separate NLR gas in virial motion, modelled with narrow Gaussian components [NC, which full width at half maximum (FWHM) has been constrained to be $\lesssim$550 km s^{-1}], from perturbed outflowing material, modelled with outflow components (OC; *FWHM* > 550 km s^{-1}; see, e.g. Figs. 1 and A.1; see also Paper I, Fig. 3). The outflow component detection has been tested considering chi-square minimisation and signal-to-noise

(S/N, see Paper I). In this paper we take advantage of SDSS spectra modelling results to construct stacked spectra and select well defined sub-samples of sources with the intention of studying NLR plasma properties in presence of AGN-driven outflows.

3. The plasma properties in the outflowing gas

Electron density and electron temperature within AGN-driven outflow regions are largely unknown. In the current literature, these quantities are important sources of uncertainty in outflow kinematic estimates for the ionised phase. Carniani et al. (2015) showed how N_e and T_e enter in the determination of the ejected mass M_{out} and, in consequence, of the mass outflow rate $\dot{M}_{out}$, kinetic and momentum powers ($\dot{E} = 0.5\dot{M}_{out}V_{out}^2$ and $\dot{P} = \dot{M}_{out}V_{out}$, respectively; V_{out} is the outflow velocity). Here we report their Eq. (5) which they derived for the [O III]λ5007 line (but the same considerations apply when Balmer emissions are used instead of [O III]; see, e.g. Cresci et al. 2015; Liu et al. 2013):

$$M_{[OIII]} = 1.7 \times 10^3 \frac{m_p C L_{[OIII]}}{10^{[O/H]-[O/H]_\odot} j_{[OIII]} \langle N_e \rangle} g, \quad (1)$$

where m_p is the proton mass, $C = \langle N_e \rangle^2 / \langle N_e^2 \rangle$ is the "condensation factor", $L_{[OIII]}$ is the [O III]λ5007 luminosity, $10^{[O/H]-[O/H]_\odot}$ is the metallicity, $j_{[OIII]}$ the oxygen emissivity. The emissivity term shows a weak dependence on electron density over several orders of magnitude, but also a relevant dependence on the electron temperature: a difference of a factor of three easily emerges when we consider T_e of 1× instead of 2×10^4 K[1]. Moreover, the outflow mass shows an inverse proportionality to the electron density.

Outflow energetics have usually been derived in the past assuming given values for electron temperature and density. While a general consensus is found for a $T_e = 1 \times 10^4$ K (e.g. Harrison et al. 2014; Carniani et al. 2015; Bischetti et al. 2017; Nesvadba et al. 2006; but see Liu et al. 2013; Cresci et al. 2015), several values are used for the electron density, spanning one order of magnitude or more: for example, 1000 cm^{-3} has been assumed by Cano-Díaz et al. (2012), 500 cm^{-3} by Carniani et al. (2015), and 100 cm^{-3} by a large number of other authors (e.g. Brusa et al. 2015; Cresci et al. 2015; Harrison et al. 2014; Kakkad et al. 2016; Liu et al. 2013).

A few diagnostic ratios involving forbidden lines can be used to derive these properties in regions with densities $\lesssim 10^6$ cm^{-3} (depending on the critical density of the involved forbidden transitions). In particular, [S II]$\lambda\lambda$6716, 6731 and [O III] flux ratio (involving [OIII]$\lambda\lambda$4959, 5007 and [OIII]λ4363) diagnostics, are potentially useful to measure N_e and T_e because of their optical wavelengths[2], through the equations:

$$T_e \approx \frac{3.29 \times 10^4}{\ln\left(\frac{R_{[OIII]}}{7.90}\right)} \text{ K}, \quad (2)$$

$$N_e = 10^2 \sqrt{T_e} \frac{R_{[SII]} - 1.49}{5.61 - 12.8 \times R_{[SII]}} \text{ cm}^{-3}, \quad (3)$$

where $R_{[OIII]} = [f(\lambda5007) + f(\lambda4959)]/f(\lambda4363)$ and $R_{[SII]} = f(\lambda6716)/f(\lambda6731)$ (Osterbrock & Ferland 2006).

[1] [O III] emissivity from PyNeb (Luridiana et al. 2015).

[2] [OII]λ3727 doublet ratio allows a further density diagnostic. However, from the observational point of view, [O II] lines are so close in wavelength that only high spectral resolution observations permit the derivation of their flux ratio. This argument precludes the use of single ionised oxygen diagnostic for the sources presented in these works.

Unfortunately, the faintness of the involved emission lines (in particular, [O III]λ4363 and [S II] doublet) and the interdependence between T_e and N_e (see Eq. (3)) make the measurement of these quantities challenging. As an example, we show in Fig. 1 (top panel) the spectrum of a source for which it is possible to model the sulphur lines well, separating OC and NC, but with faint [O III]λ4363. In this case, therefore, it is possible to derive $R_{[SII]}$ but not $R_{[OIII]}$. The bottom panel of Fig. 1 shows instead how the vicinity of sulphur and oxygen lines with broad line region (BLR) Balmer emission Hα and Hγ in type 1 AGNs also complicates the situation. These are the reasons for which, for example, Vaona et al. (2012) derived reliable estimates of the electron temperature of the unperturbed NLR gas only for ∼500 objects, starting from a parent sample of ∼2500 SDSS AGNs.

The fact that the OC can be fainter than the unperturbed narrow components (see Paper I, Fig. C.1), makes it even more difficult to derive such diagnostic information for the outflowing ionised material. Only for a handful of previous studies was it possible to derive such physical properties, although with large uncertainties. These works are generally based on single luminous targets (e.g. Brusa et al. 2016; Perna et al. 2015a) or, in the best cases, on a small number of sources (e.g. Westmoquette et al. 2012). Harrison et al. (2012) used a stacked spectrum of $z \sim 2.4$ ultra-luminous galaxies to estimate the electron density. Genzel et al. (2014), assuming a pressure equilibrium between outflowing gas and the ionised gas in star-forming regions, proposed an electron density of ∼80 cm^{-3} for the outflowing gas, as derived from star-forming ionised gas in the discs and centres of star-forming galaxies at $z \sim 2$ (see also Kaasinen et al. 2017). These few results point to large ranges of values for the electron densities, from $\approx 10^2$ to $>10^3$ cm^{-3} (see, e.g. Rodríguez Zaurín et al. 2013). To the best of our knowledge, the electron temperature has been derived for only six targets (those presented by Villar-Martín et al. 2014; Nesvadba et al. 2008; and Brusa et al. 2016), with $T_e \approx 1.5 \times 10^4$ K.

3.1. Electron temperature diagnostics

To constrain at best the electron temperature in ionised gas in our X-ray/SDSS selected AGN sample, we use two different approaches. With the first approach, we constructed a stacked spectrum to derive temperature-sensitive diagnostic ratio R_{OIII} for both unperturbed and outflow emitting gas. Then, we considered well selected individual objects and derived the same quantity to verify the reliability of the results found with the former approach.

Our X-ray/SDSS sample shows a large variety of AGN types, from typical type 1 AGNs with blue spectra and prominent BLR lines to reddened and/or faint AGNs (see Paper I, Fig. 3). Because of the not-so-large number of X-ray/SDSS sources, instead of stacking galaxies in bins of AGN luminosity and/or obscuration, we chose to stack continuum-subtracted spectra. We considered only those sources for which we were able to model the continuum over the entire wavelength range covering the separation between the doubly ionised oxygen lines using pPXF best-fit technique (Paper I). From these, we constructed the stacked spectrum combining the continuum-subtracted spectra of all those sources with evidences of outflow in the [O III] line (75 AGNs). These sources are associated with faint and/or obscured AGNs ($10^{40} < L_{[OIII]} < 10^{42.5}$, with a median luminosity of $10^{41.2}$ erg/s); this allowed us to reduce the possible H$\gamma\lambda$4342 BLR emission in the vicinity of [O III]λ4363.

Figure 2 shows the median stacked spectrum and the best-fit results we obtain fitting simultaneously all the prominent

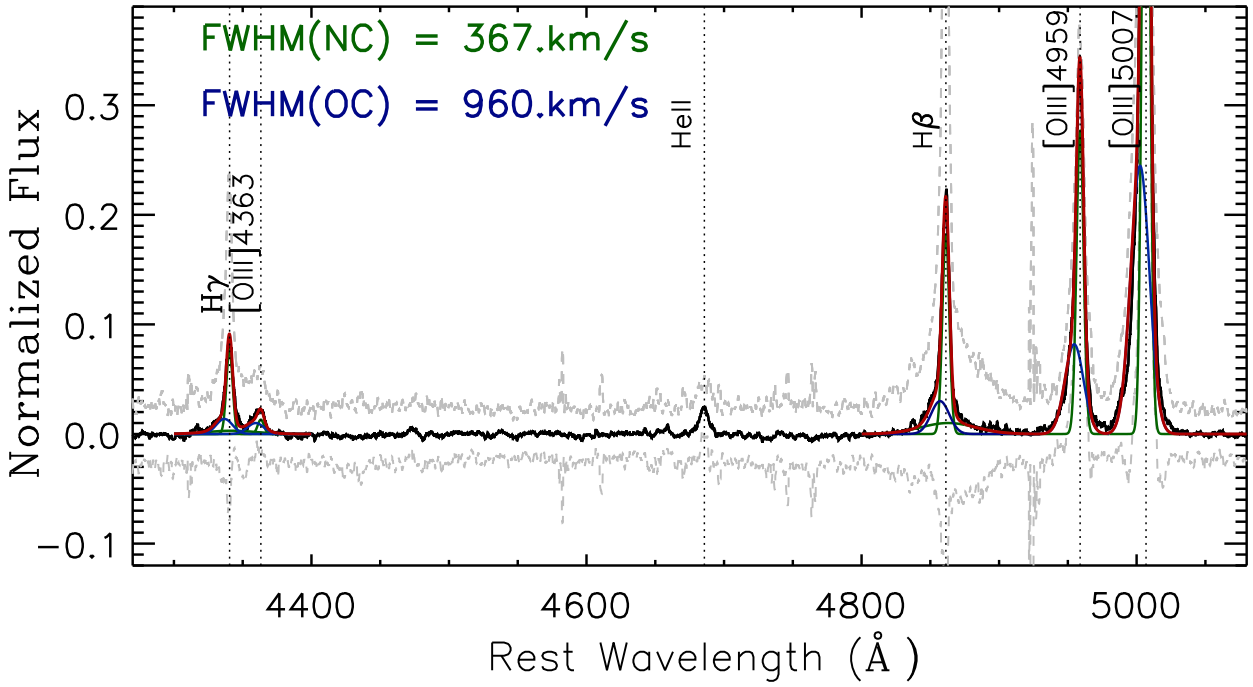

Fig. 2. Median stacked spectrum around the doubly ionised oxygen emission lines obtained combining the spectra of faint/obscured sources with evidence of ionised outflows (see the text for more details). Dashed curves highlight 1σ uncertainties. Red curve represents the best-fit result we obtained fitting simultaneously the emission lines displayed. Green Gaussian represent NC and BC components, blue profiles mark OC.

features in the displayed wavelength range and following the strategy presented in Paper I. The presence of outflow components with $FWHM \approx 1000$ km s^{-1} is noticeable in all displayed emission lines. From simultaneous multicomponent fit, we derived the flux ratios $R_{[OIII]}(NC)_{stack} = 100^{+60}_{-30}$ and $R_{[OIII]}(OC)_{stack} = 33^{+74}_{-8}$ (the errors are computed employing a bootstrap method; Peterson et al. 2004).

The stacked spectrum allowed us also to check for the possible presence of [Fe II] contamination of [O III]λ4363. In fact, Curti et al. (2017) found that faint iron lines at 4288 Å and 4360 Å concomitantly emerge in high-metallicity stack galaxy spectra, resulting in an overestimation of the oxygen line flux. The absence of [Fe II]λ4288 permitted us to reasonably exclude the possible contribution of iron contamination of oxygen 4363 Å line.

With the second approach, we carefully select a sample of sources with well detected and unblended [O III]λ4363 line from the total X-ray/SDSS sample. To allow the analysis of the outflow wings in such faint emission line we narrowed down the sample selecting only those targets with well detected ($S/N >$ 10) [O III]λ4363. Furthermore, to mitigate blending problems, we discarded all those sources with broad Hγ BLR profiles after a visual inspection. This reduced the sample to eight sources. For each target, we fitted simultaneously the oxygen line at 4363 Å and the Balmer line at 4342 Å imposing the same systemics, widths and sets of Gaussian components as obtained from the simultaneous fit in the Hα and Hβ regions (Paper I). From such analysis, we derived R_{OIII} flux ratios for both the NC and OC components.

For sources without evidence of outflows in [O III]λ5007, the spectral analysis does not require any decomposion between NC and OC emission; we could therefore relax the requirement on the S/N, imposing a $S/N > 5$, and derive temperature-sensitive flux ratios also for this sub-sample. In this way we obtained $R_{[OIII]}(NC)$ ratios for an additional ten AGNs. The spectra around the region of [O III]λ4363 and the fit results for these eight plus ten sources are reported in Fig. 3. The derived R_{OIII} distributions for NC (18 AGNs) and OC (8 AGNs) are shown in Fig. 4 (left panel).

We note that the $R_{OIII}(OC)$ distribution is located closely around the median position of that of $R_{OIII}(NC)$ (i.e. $R_{OIII} \sim 90$). This could suggest that, on average, NC and OC share similar electron temperatures (Eq. (2)). These samples are however very small to point to any conclusion. We therefore tested this thesis using additional 26 targets with [O III]λ4363 detected with $5 < S/N < 10$ and showing evidence of ionised outflows. If we assume the same temperature for both outflowing and systemic ionised gas, the amplitude fractions OC/NC should be the same in [O III]λ5007 and [O III]λ4363 (see Eq. (2)). We fitted the emission lines with this additional constrain. The fit results are shown in the last part of Fig. 3. All the temperature-sensitive flux ratios are reported in Table A.2.

We note that the profiles are generally well reproduced under the assumption that $T_e(NC) = T_e(OC)$. Of course, the low quality of the spectra does not allow a strong result significance. In Fig. 4, left, we show the distribution obtained adding these 26 targets to the outflow sample. In the figure, we also show the results from the stack analysis; the overlap between 68% confidence intervals for NC and OC flux ratios also tends to support our assumption in deriving the distribution of flux ratio measurements from single targets. From the final distribution, we derive the median value $\langle R_{[OIII]}(NC)\rangle = \langle R_{[OIII]}(OC)\rangle = 55 \pm 28$, with the uncertainty defined by the 68% confidence interval.

All median flux ratios obtained so far are collected in Table 1.

3.2. Electron density diagnostics

As in the previous section, we used two different approaches to derive the electron density of AGN-ionised gas. We first constructed a stacked spectrum combining the spectra of all those

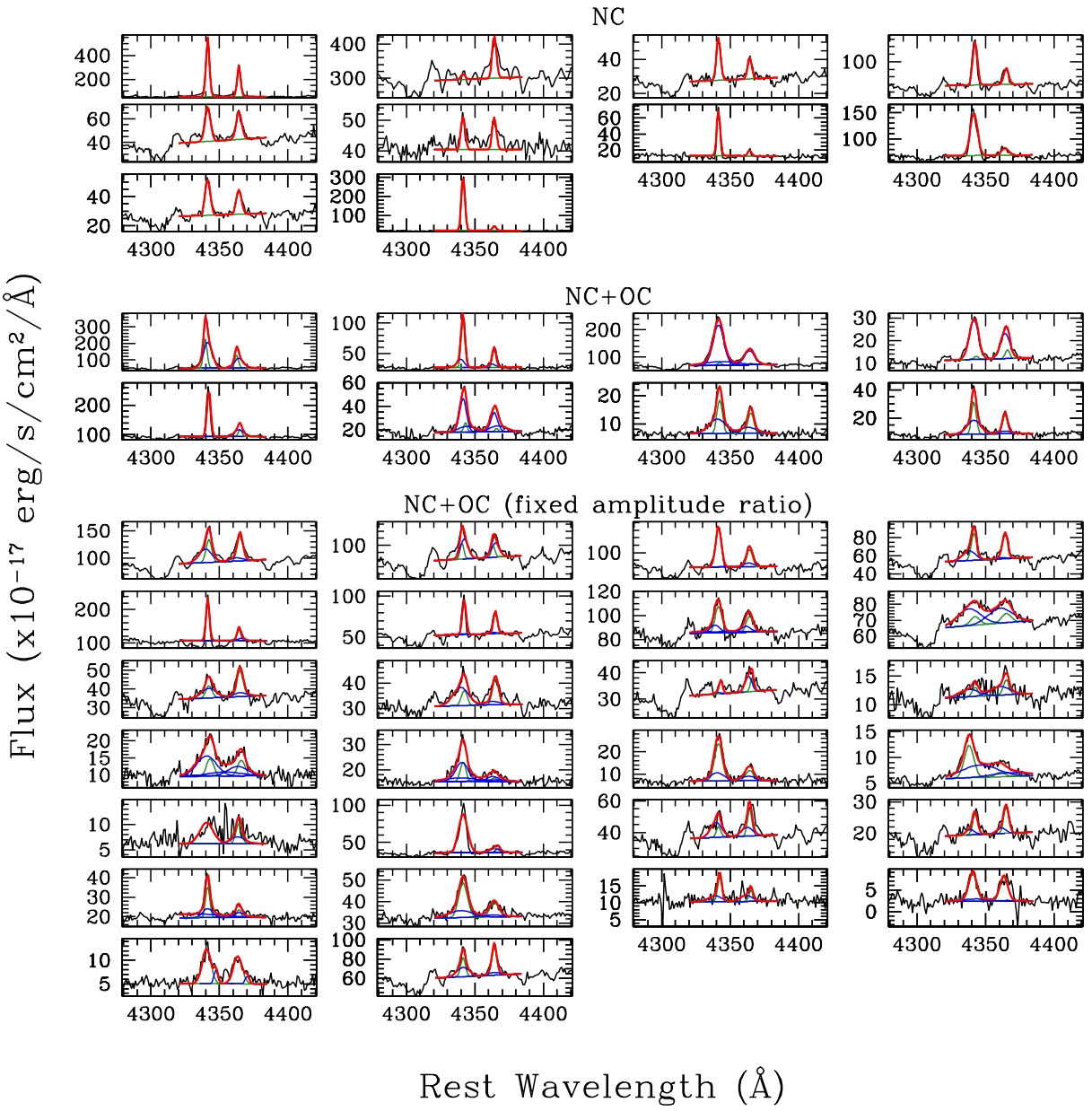

Fig. 3. Magnification of the region of [O III]λ4363-H$\gamma\lambda$4342 lines for the 44 sources for which we could determine $R_{[OIII]}$ flux ratios. For each spectrum, the best-fitting components presented in Sect. 3.1 are superimposed: solid green curves represent the systemic narrow component (NC); blue curves the OC.

sources with evidence of ionised [O III]λ5007 outflows and without blending problems between sulphur and Hα BLR emission. For each spectrum satisfying such conditions (90 AGNs), we subtracted the continuum emission and normalised the fluxes to the Hα peak. Figure 5 shows the median stacked spectrum obtained combining the normalised, continuum-subtracted spectra. In order to best model the sulphur profile and distinguish between systemic and perturbed emitting gas, we fitted simultaneously Hα, [N II] and [S II] lines (see Paper I for further details). We clearly reveal and separate OC, with *FWHM* $\approx$ 800 km s^{-1}, from a narrower unperturbed component, with FWHM of $\approx$350 km s^{-1}, in all emission lines. From the best-fit results (shown in Fig. 5), we derive $R_{[SII]}(NC)_{stack} = 1.12^{+0.06}_{-0.04}$ and $R_{[SII]}(OC)_{stack} = 0.91^{+0.16}_{-0.19}$ (as before, the errors were computed employing a bootstrap method).

The second approach employed the analysis of optical spectra of single objects. As a first step, we measured the NLR diagnostic ratio $R_{[SII]}$ for all AGNs with no severe and ambiguous blending with Hα BLR emission and without signatures of outflows revealed in simultaneous fits, resulting in a sample of 121 AGNs. In fact, when OC components are revealed, the doublet lines are usually severely blended and, in general, the fitting procedure gives ambiguous results (see, e.g. Perna et al. 2015a; Rodríguez Zaurín et al. 2013; Villar-Martín et al. 2014). From this sample we obtained the distribution shown in Fig. 4, right (grey histogram).

To study the electron density of the outflowing regions, we focussed the analysis on those AGNs with the simplest spectral profiles, meaning those with well defined [S II] wings, modelled with two kinematic components (NC + OC). and, as before, without strong blending with BLR emission. In Paper I we noticed that approximately 40% of X-ray/SDSS AGNs of our parent sample display signatures of ionised outflows. The above mentioned conditions are, however, satisfied by only 28 sources.

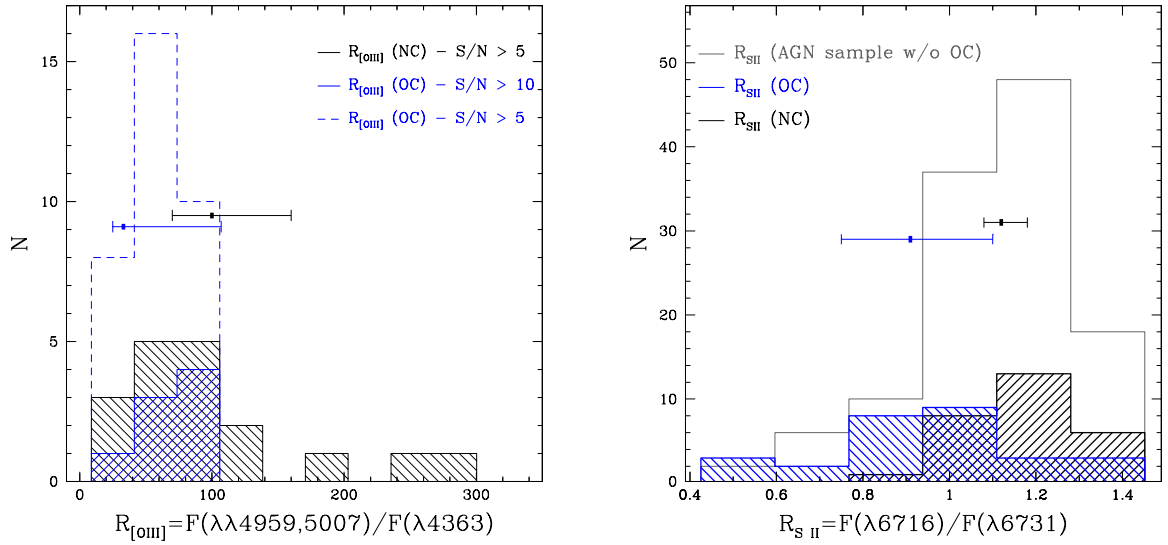

Fig. 4. *left*: [O III] ratio distributions. Grey shaded areas mark the $R_{[OIII]}$ distribution for the unperturbed ionised gas (i.e. NC). Blue shaded area denotes the outflow emission $R_{[OIII]}$ distribution of $S/N > 10$ sources. The blue dashed line shows the $R_{[OIII]}$ histogram of the outflow components of all $S/N > 5$ sources (see the text for detailed analysis description). In each panel, median and 68% confidence intervals obtained from the analysis of stacked spectra are also shown for comparison (black and blue symbols, representing line ratios associated with NC and OC, respectively). *Right*: [S II]$\lambda\lambda$6716, 6731 ratio distributions. The grey solid line marks the distribution for the AGN sample without evidence of outflows from our line fitting routine. The black and blue shaded areas denote the distributions for NC and OC sulphur ratios obtained from the sub-sample of 28 AGNs.

Table 1. Plasma properties.

	Stacked			Individual		
	NC	OC	(#)	NC	OC	(#)
	(1)	(2)	(3)	(4)	(5)	(6)
$R_{[SII]}$	$1.12^{+0.06}_{-0.04}$	$0.91^{+0.16}_{-0.19}$	(90)	$1.16^{+0.16}_{-0.17}$	$0.94^{+0.27}_{-0.24}$	(28)
$R_{[OIII]}$	100^{+60}_{-30}	33^{+74}_{-8}	(75)	55^{+28}_{-28}	55^{+28}_{-28}	(34)
N_e	550^{+110}_{-130} cm^{-3}	1200^{+1500}_{-500} cm^{-3}	(90)	480^{+450}_{-300} cm^{-3}	1100^{+1900}_{-750} cm^{-3}	(28)
T_e	$1.3^{+0.2}_{-0.2} \times 10^4$ K	$2.3^{+0.6}_{-1.0} \times 10^4$ K	(75)	$1.7^{+1.1}_{-0.3} \times 10^4$	$1.7^{+1.1}_{-0.3} \times 10^4$ K	(34)

Notes. Median estimates for sulphur and oxygen line ratios (first two rows) and electron density and temperature (third and fourth rows), for both narrow (NC) and outflow components (OC). Columns (1) and (2) show the results obtained from the analysis of median stacked spectra constructed collecting # [Col. (3)] spectra. Columns (4) and (5) display the median results obtained analysing sub-samples of # [Col. (6)] individual objects. The oxygen flux ratio and electron temperature obtained from the analysis of individual targets are obtained under the assumptions described in the text, and are referred to both NC and OC.

This reflects the difficulties in the electron density measurements. The fitted spectra are shown in Fig. A.1. From this sample, we computed $R_{[SII]}$ ratios for both NC and OC. The $R_{[SII]}$(NC) distribution (Fig. 4, right) has a smaller spread when compared with that of the AGN sample without OC components, because of the particular selection. Instead, the $R_{[SII]}$(OC) distribution (blue area) covers a larger range of values and is peaked at lower ratios. From these distributions, we derived the median values $\langle R_{[SII]}(NC)\rangle = 1.16^{+0.16}_{-0.17}$ and $\langle R_{[SII]}(OC)\rangle = 0.94^{+0.27}_{-0.24}$ (the errors define 68% confidence intervals; see Table A.1 for the compilation of all flux ratio measurements).

From each [S II] intensity ratio, in principle, we could derive an estimate of the electron density from Eq. (3), taking into account the dependence on the electron temperature. This means that for each source, in order to derive at best N_e, we should be able to detect and analyse all the emission lines needed for electron density and temperature diagnostics. Unfortunately, the faintness of the temperature-sensitive emission line [O III]λ4363 does not allow spectral analysis for all but seven of our targets selected to study the [S II] emission (see, e.g. the spectrum in Fig. 1, panel a). Therefore, we chose to follow a statistical approach, and derive median electron densities of outflowing and systemic gas for given median electron temperatures.

3.3. Results: the plasma properties

We compute fiducial estimates of the electron temperatures of both NC and OC through Eq. (2), using the median doubly ionised oxygen flux ratios derived from stack analysis, $T_e(NC) = (1.3 \pm 0.2) \times 10^4$ K and $T_e(OC) = 2.3^{+0.6}_{-1.0} \times 10^4$ K. We also use the median value of the final $R_{[OIII]}$ distribution (Fig. 4, left, blue dashed histogram), to derive an additional estimate of the electron temperature in the outflow region, $T_e(OC) = 1.7^{+1.1}_{-0.3} \times 10^4$ K. Because of the similarities in the distributions of NC and OC, and the fact that this temperature value is also consistent within $\sim 1\sigma$ with the stack analysis measurements, we consider $T_e = 1.7 \times 10^4$ K as a median electron temperature for the entire NLR emitting gas (i.e. NC and OC emitting material).

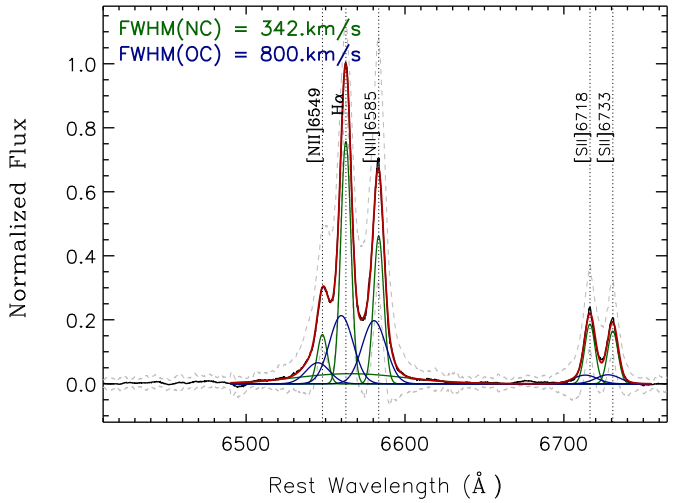

Fig. 5. Median stacked spectrum around the [S II] emission line doublet obtained combining the spectra of sources with evidence of ionised outflows and without blending problems with Hα BLR emission. Dashed curves highlight 1σ uncertainties. The red curve represents the best-fit result we obtained fitting simultaneously Hα, [N II] and [S II] doublets. The green Gaussians represent NC and BC components, blue profiles mark OC.

We therefore adopt such median temperature to derive fiducial electron densities from Eq. (3), for both best-fit NC and OC results obtained from stack analysis: $N_e^{stack}(NC) = 550^{+130}_{-110}$ cm^{-3} and $N_e^{stack}(OC) = 1200^{+1500}_{-500}$ cm^{-3}. In the same manner, we also derive fully consistent electron densities from the median values of sulphur ratio distributions: $\langle N_e(NC)\rangle = 480^{+450}_{-300}$ cm^{-3} and $\langle N_e(OC)\rangle = 1100^{+1900}_{-750}$ cm^{-3}[3].

The targets we used to construct the stacked spectra have observed [O III]λ5007 luminosity range of $10^{40} \lesssim L_{[OIII]} \lesssim 10^{42.5}$, with a median luminosity of $10^{41.2}$ erg/s, similarly to those of the individual spectra reported in Tables A.1 and A.2. Because of their faint and/or obscured nature, we also report the median values of doubly ionised luminosity corrected for the extinction, $L^{int}_{[OIII]} \sim 10^{41.6}$ erg/s (derived using Balmer decrement arguments and assuming Case B ratio of 3.1 and the SMC dust-reddening law; Perna et al. 2015a) and of the intrinsic X-ray luminosity, $L_X \sim 10^{42.5}$ erg/s. The limitation in AGN luminosity regime is due to the above mentioned conditions required to analyse [S II] and [O III]λ4363 which, for instance, preclude the inclusion of the majority of unobscured type 1 AGNs. Therefore, we note that the results presented here may be relevant only to characterise the outflow plasma properties of faint and moderately luminous AGNs ($10^{40.5} \lesssim L_X \lesssim 10^{44}$, or $10^{41.2} \lesssim L^{int}_{[OIII]} \lesssim 10^{42}$).

Narrow component plasma properties have been derived for larger samples of SDSS Seyferts by other authors in the past decade (e.g. Zhang et al. 2013; Vaona et al. 2012). Our estimates are totally consistent with the median values indicated by these authors ($N_e \approx 400$ and $T_e \approx 1.5 \times 10^4$ K).

Although with large uncertainties, the outflow plasma condition estimates presented in this work are, to the best of our knowledge, the first average estimate from stack analysis and medium-size samples (≈30 targets) of AGNs. Moreover, despite the fact that our median values for N_e(NC) and N_e(OC) are still comparable within the errors, our analysis suggests that the outflowing gas may actually be characterised by a large range of electron densities, possibly favouring the high-density regime. As a consequence, the most common assumption to derive outflow energetics ($N_e = 100$ cm^{-3}) may overestimate such measurements even by a factor of ten.

[3] Similar results are obtained for the seven sources for which we were able to analyse both doubly ionised oxygen lines and sulphur lines (see Sect. 3.2): $\langle N_e(NC)\rangle = 510$ cm^{-3} and $\langle N_e(OC)\rangle = 1100$ cm^{-3}.

3.4. Possible bias in T_e due to [O III]λ4363 selection

The fact that we compute the electron temperature for those sources with intense [O III]λ4363 could bias the results obtained with the second approach, by favouring targets with higher T_e (Eq. (2)). We compute 1σ upper limits for all those sources without clear detection and, from the median value of their R_{OIII} distribution, we derive an upper limit on the electron temperature of ≈3×10^4 K. Unfortunately, this value is not useful to our purpose. However, the fact that we have not observed any difference in the median T_e between the $S/N > 10$ and $5 < S/N < 10$ samples could suggest that the bias is, if any, negligible. The same behaviour can be seen for the large sample studied by Zhang et al. (2013), for which the same NLR unperturbed gas electron temperature has been found for both their two [O III]λ4363 luminosity subclasses of Seyferts. Indeed, the scarce relevance of bias may be also stressed by the consistent results we obtained from stack analysis, for which only faint and obscured AGNs have been taken into account.

4. Outflowing gas ionisation mechanisms

The unambiguous separation between NC and OC components in the [S II] emission lines for the medium size sample of the 28 AGNs from which we derived electron density estimates, enables the study of the diagnostic diagrams [O III]/Hβ versus [S II]/Hα (see, e.g. Kewley et al. 2006). Furthermore, we find well detected [O I]λ6300 emission lines in all sources (see Fig. A.1). Therefore, taking advantage from simultaneous analysis results, we fit this faint emission constraining the systemics and the FWHM of NC and OC components and derive the intensity ratio needed for a second diagnostic diagram, [O III]/Hβ vs. [O I]/Hα (Kewley et al. 2006).

Figure 6 shows three diagnostic diagrams, [O III]/Hβ versus [N II]/Hα (already presented in Paper I for the entire sample of X-ray/SDSS AGNs), [S II]/Hα and [O I]/Hα for both NC and OC. The lines drawn in the diagrams correspond to the optical classification scheme of Kewley et al. (2006, 2013): in the second and third diagram, the LINER locus is shown. The OC appears associated with the same level of ionisation of NC (i.e. same [O III]/Hβ ratios) and similar [N II]/Hα but larger [S II]/Hα and [O I]/Hα ratios. The second and third diagnostic diagrams clearly point to a LINER-like emission for the outflow components. Such line ratios are generally associated with ionisation by fast radiative shocks (e.g. Allen et al. 2008; but see also Belfiore et al. 2016). Shock model results have been made available for a large range of physical parameters: pre-shock density N_e^{pre} (to be distinguished by electron density we measured previously, and possibly associated with "post-shock" regions; see, e.g. Harrison et al. 2012), shock velocity, magnetic field, and abundances. We superimposed on the figure a grid of shock model with assumed solar abundance and a pre-shock density of 100 cm^{-3} (ITERA; Groves & Allen 2010). The grid shows different line ratios for various values of magnetic field and shock velocities (up to 1000 km s^{-1}). The models, however, fail to reproduce the exact position of the OC line ratios in the

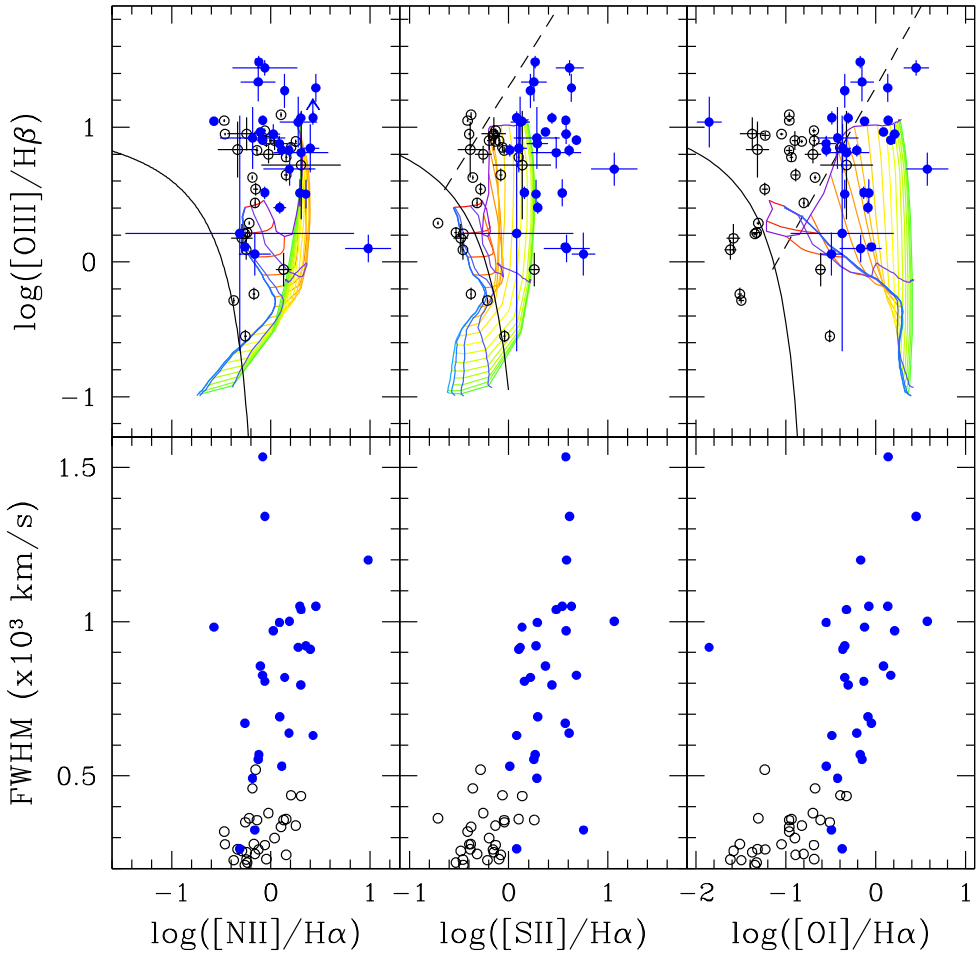

Fig. 6. *Top panels*: [O III]/Hβ versus [N II]/Hα, [S II]/Hα and [O I]/Hα BPT diagrams for the 28 sources used to derive the outflow electron density. Solid and dashed black lines represent the curve used to separate the purely SF galaxies, AGNs and LINER loci. Shock model grids are overplotted, with increasing velocities, from 100 to 1000 km s^{-1} (red to green lines), and magnetic field (blue to purple curves). *Bottom panels*: FWHM plotted against log([N II]/Hα), log([S II]/Hα), and [O I]/Hα *from left to right*. Both NC (open black) and OC (solid blue symbols) are shown. Positive correlations are found between the three ionisation state and the gas kinematics tracers.

BPT diagrams. We tested all available shock models from the ITERA library without any improvement.

It is possible that more extreme set of parameters are needed to reproduce the shocks in AGN-driven outflows: under particular assumptions, shock velocities and gas velocity dispersion can be similar, and therefore even larger than 1000 km s^{-1} (see McElroy et al. 2015, discussion). Radiation pressure-dominated photo-ionisation models easily reproduce the loci occupied by NC measurements (see the model grids in Westmoquette et al. 2012) but, as the shock models, fail to cover the highest [O I]/Hα and [S II]/Hα ratios. We notice however that these values might also be related to the presence of high metallicity regions within outflowing gas (see Villar-Martín et al. 2014), and that further observational efforts and theoretical investigation are required to discriminate between radiation pressur and shock models.

More strong evidence for shock excitation interpretation is given by the observed correlation between the gas kinematics and ionisation state (Dopita & Sutherland 1995). The line ratios produced in photo-ionised regions should be independent of the gas kinematics, while are expected to correlate with the kinematics of the shock-ionised material (see McElroy et al. 2015; Ho et al. 2014; Arribas et al. 2014). In the lower panels of Fig. 6 we show the FWHM against [N II]/Hα, [S II]/Hα and [O I]/Hα ratios for both NC and OC. We note that the FWHM should not suffer for strong degeneracy between the [S II] doublet and [N II]-Hα complex components, because derived from our simultaneous fits (Fig. A.1). We use Spearman rank correlation coefficients to determine the significance of the observed trends between line ratios and velocities. We find, on average, coefficients of $\approx$0.45 with probabilities of $\lesssim$0.01 for the correlation being observed by chance, for both NC and OC separately. The same correlation has been found by Arribas et al. (2014) for NC (but not for OC), confirming the complex kinematic conditions within the NLR.

5. Discussion and conclusions

In Perna et al. (2017), we analysed SDSS optical and X-ray spectra of a sample of 563 AGN at $z < 0.8$. In this paper, we have taken advantage of the optical spectra modelling presented in Paper I to derive the plasma properties for both narrow line and outflowing component emission. For the first time we derived estimates of electron temperature and density of the outflowing gas from stack analysis and medium size samples ($\approx$30) of faint and moderately luminous AGNs.

Studying individual AGN spectra, we found indications suggesting that T_e may be quite similar in both outflowing and unperturbed gas, with a median value $T_e = 1.7^{+1.1}_{-0.3} \times 10^4$ K. The analysis of a stacked spectrum derived combining the spectra of faint and obscured X-ray detected AGNs allowed the determination of independent estimates for both NC and OC: $T_e(\mathrm{NC}) = 1.3 \times 10^4$ K and $T_e(\mathrm{OC}) \approx 2.4 \times 10^4$ K. These values are still consistent (within 1σ) with the median value obtained from individual spectra analysis.

In Sect. 4 we presented BPT and ionisation state – velocity diagnostics diagrams for 28 AGNs selected from the X-ray/SDSS sample; such diagnostics indicate a shock excitation interpretation for the observed ionised outflows. If this is the case, the similar electron temperature of OC and NC could be consistent with theoretical arguments, which postulate that the (forward) shock accelerating the ISM gas is strongly cooled, so that the gas temperature rapidly returns to its pre-shock value (King 2014; see also its Fig. 2). However, if the bulk of emission is associated to shock excitation, we should observe much higher temperatures ($T_e > 5 \times 10^5$ K; Osterbrock & Ferland 2006). These temperatures are ruled out by our observations: in that case, we should observe much stronger [O III]λ4363 lines. Even considering possible dust extinction effects, which could affect the doubly ionised oxygen line ratios of a factor of 0.85 (assuming a SMC dust-reddening law; Prevot et al. 1984), our temperature estimates would be just ∼10% higher.

The position of OC component flux ratios in the BPT may also be associated with different physical origins. For example, the high [S II]/Hα and [O I]/Hα OC ratios can be associated with hard ionisation radiation field, assuming the material is close to the AGN, or with high metallicities (e.g. Belfiore et al. 2016; Villar-Martín et al. 2014). Moreover, the kinematic separation between different emission line components does not ensure a common spatial distribution for all the emitting species in diagnostic diagrams. Hence, different emitting species could be characterised by distinct physical conditions. Spatially resolved information is required to better investigate the ionisation source of outflowing gas. The outflowing gas electron densities we derived analysing individual targets and a stacked spectrum displayed a wide range of values, with a distribution characterised by a median value of ≈1200 cm^{-3} and a 68% interval going from 700 to 3000 cm^{-3} (Table 1).

Xu et al. (2007) studied the NLR emission of ∼100 SDSS type 1 AGNs. They observed a negative trend between the electron density and the blueshift of the [O III] wing. This result conflicts with our measurements. However, we note that all these results are currently limited to small number of sources: the trend suggested by Xu et al. (2007) is based on the measurement of low N_e in 6 out 54 targets with signature of outflows. Moreover, they derived electron density estimates without any separation between narrow and outflow components, making the comparison difficult.

On the other hand, other indications in literature suggest even higher N_e in the outflowing regions: Villar-Martín et al. (2015), studying high-ionisation lines such as [Fe X] and [Ne V], proposed electron densities up to 10^5 cm^{-3}. However, such emission lines, although actually tracing outflowing gas (see, e.g. Lanzuisi et al. 2015), have high ionisation potential and critical densities (IP $\gtrsim$ 100 eV and $N_c \gtrsim 10^7$ cm^{-3}, to be compared to sulphur IP = 10.36 and $N_c \approx 2500$ cm^{-3}). They could be associated with more internal regions (see Rose et al. 2015a,b, in which such lines have been proposed to occupy a region between the BLR and the inner walls of the torus; see also Morse et al. 1998). When we consider kpc-scale outflows, typical electron density may be instead more similar to those of narrow emission lines in NLR rather than in the nuclear regions. The slightly higher density (≈1200 instead of ≈500 cm^{-3}) may be explained by a possible compression due to the AGN wind on the ISM material.

In summary, all these considerations based on the results we obtained and on speculative arguments, suggest a more conservative approach in the estimate of the outflow energetics: the most typical assumption in deriving crucial outflow energetics (i.e. $N_e = 100$ cm^{-3}) may, in fact, overestimate the outflow energetics by a factor of up to ten.

Acknowledgements. M.P., G.L. and M.B. acknowledge support from the FP7 Career Integration Grant "eEASy" ("SMBH evolution through cosmic time: from current surveys to eROSITA-Euclid AGN Synergies", CIG 321913). G.L. acknowledges financial support from ASI-INAF I/037/12/0. Support for this publication was provided by the Italian National Institute for Astrophysics (INAF) through PRIN-INAF-2014 ("Windy Black Holes combing galaxy evolution"). We thank the anonymous referee for his/her constructive comments to the paper. M.P. thanks A. Citro and S. Quai for useful discussion on stacked spectra analysis. Funding for the Sloan Digital Sky Survey (SDSS) has been provided by the Alfred P. Sloan Foundation, the Participating Institutions, the National Aeronautics and Space Administration, the National Science Foundation, the US Department of Energy, the Japanese Monbukagakusho, and the Max Planck Society. The SDSS Web site is http://www.sdss.org/. The SDSS is managed by the Astrophysical Research Consortium (ARC) for the Participating Institutions. The Participating Institutions are The University of Chicago, Fermilab, the Institute for Advanced Study, the Japan Participation Group, The Johns Hopkins University, Los Alamos National Laboratory, the Max-Planck-Institute for Astronomy (MPIA), the Max-Planck-Institute for Astrophysics (MPA), New Mexico State University, University of Pittsburgh, Princeton University, the United States Naval Observatory, and the University of Washington.

References

Allen, M. G., Groves, B. A., Dopita, M. A., et al. 2008, ApJS, 178, 20
Arribas, S., Colina, L., Bellocchi, E., et al. 2014, A&A, 568, A14
Belfiore, F., Maiolino, R., Maraston, C., et al. 2016, MNRAS, 461, 3111
Bischetti, M., Piconcelli, E., Vietri, G., et al. 2017, A&A, 598, A122
Brusa, M., Bongiorno, A., Cresci, G., et al. 2015, MNRAS, 446, 2394
Brusa, M., Perna, M., Cresci, G., et al. 2016, A&A, 588, A58
Cano-Díaz, M. R., Marconi, A., Netzer, H., Shemmer, O., & Cresci, G. 2012, A&A, 537, L8
Carniani, S., Marconi, A., Maiolino, R., et al. 2015, A&A, 580, A102
Cappellari, M. 2017, MNRAS, 466, 798
Cappellari, M., & Emsellem, E. 2004, PASP, 116, 138
Cresci, G., Mainieri, V., Brusa, M., et al. 2015, ApJ, 799, 81
Curti, M., Cresci, G., Mannucci, F., et al. 2017, MNRAS, 465, 1384
De Robertis, M. M., & Osterbrock, D. E. 1986, ApJ, 301, 727
Dopita, M. A., & Sutherland, R. S. 1995, ApJ, 455, 468
Feruglio, C., Fiore, F., Carniani, S., et al. 2015, A&A, 583, A99
Fiore, F., Feruglio, C., Shankar, F., et al. 2017, A&A, 601, A143
Georgakakis, A., Coil, A. L., Willmer, C. N. A., et al. 2011, MNRAS, 418, 2590
Genzel, R., Förster Schreiber, N. M., Rosario, D., et al. 2014, ApJ, 796, 7
Groves, B., & Allen, M. 2010 ArXiv e-prints [arXiv:1002.3372G]
Harrison, C. M., Alexander, D. M., Swinbank, A. M., et al. 2012, MNRAS, 426, 1073
Harrison, C. M., Alexander, D. M., Mullaney, J. R., et al. 2014, MNRAS, 441, 3306
Ho, I. T., Kewley, L. J., Dopita, M. A., et al. 2014, MNRAS, 444, 3894
Hopkins, P. F., Hernquist, L., Cox, T. J., & Kereš, D. 2008, ApJS, 175, 356
Husemann, B., Scharwächter, J., Bennert, V. N., et al. 2016, A&A, 594, A44
Jin, C., Ward, M., Done, C., et al. 2012, MNRAS, 420, 1825
Kaasinen, M., Bian, F., Groves, B., et al. 2017, MNRAS, 465, 3220
Kakkad, D., Mainieri, V., Padovani, P., et al. 2016, A&A, 592, A148
Kewley, L. J., Groves, B., Kauffmann, G., & Heckman, T. 2006, MNRAS, 372, 961
Kewley, L. J., Maier, C., Yabe, K., et al. 2013, ApJ, 774, L10
King, A. 2014, Space Sci. Rev., 183, 427
King, A., & Pounds, K. 2015, ARA&A, 53, 115
Lanzuisi, G., Perna, M., Delvecchio, I., et al. 2015, A&A, 578, A120
Liu, G., Zakamska, N. L., Greene, J. E., et al. 2013, MNRAS, 436, 2576
Luridiana, V., Morisset, C., & Shaw, R. A. 2015, A&A, 573, A42
McElroy, R., Croom, S. M., Pracy, M., et al. 2015, MNRAS, 446, 2186

Menci, N., Fiore, F., Puccetti, S., & Cavaliere, A. 2008, ApJ, 686, 219
Morse, J. A., Cecil, G., Wilson, A. S., & Tsvetanov, Z. I. 1998, ApJ, 505, 159
Nesvadba, N. P. H., Lehnert, M. D., Eisenhauer, F., et al. 2006, ApJ, 650, 693
Nesvadba, N. P. H., Lehnert, M. D., De Breuck, C., et al. 2008, A&A, 491, 407
Osterbrock, D. E., & Ferland, G. J. 2006, Astrophysics of Gaseous Nebulae and Active Galactic Nuclei (University Science Books)
Perna, M., Brusa, M., Cresci, G., et al. 2015a, A&A, 574, A82
Perna, M., Brusa, M., Salvato, M., et al. 2015b, A&A, 583, A72
Perna, M., Lanzuisi, G., Brusa, M., Mignoli, M., & Cresci, G. 2017, A&A, 603, A99 (Paper I)
Peterson, B. M., Ferraresi, L., Gilbert, K. M., et al. 2004, ApJ, 613, 682
Prevot, M. L., Lequeux, J., Prevot, L., et al. 1984, A&A, 132, 389
Rice, M. S., Martini, P., Greene, J. E., et al. 2006, ApJ, 636, 654
Rodríguez Zaurín, J., Tadhunter, C. N., Rose, M., & Holt, J. 2013, MNRAS, 432, 138
Rose, M., Elvis, M., & Tadhunter, C. 2015a, A&AS, 144, 24
Rose, M., Elvis, M., & Tadhunter, C. 2015b, MNRAS, 448, 2900
Rupke, D. S. N., & Veilleux, S. 2013, ApJ, 768, 75
Sijacki, D., Vogelsberger, M., Genel, S., et al. 2015, MNRAS, 452, 575
Trichas, M., Green, P. J., Constantin, A., et al. 2013, ApJ, 778, 188
Vaona, L., Coroi, S., Di Mille, F., et al. 2012, MNRAS, 427, 1266
Villar-Martín, M., Emonts, B., Humphrey, A., et al. 2014, MNRAS, 440, 3202
Villar-Martín, M., Bellocchi, E., Stern, J., et al. 2015, MNRAS, 454, 439
Wang, J., & Xu, D. W. 2015, A&A, 573, A15
Westmoquette, M. S., Clements, D. L., Bendo, G. J., & Khan, S. A. 2012, MNRAS, 424, 416
Wu, J., Vanden Berk, D., Grupe, D., et al. 2012, ApJS, 201, 10
Xu, D., Komossa, S., Zhou, H., et al. 2007, ApJ, 670, 60
Zakamska, N. L., & Greene, J. E. 2014, MNRAS, 442, 784
Zhang, Z. T., Liang, Y. C., & Hammer, F. 2013, MNRAS, 430, 2605
Zubovas, K., & King, A. R. 2014, MNRAS, 439, 400

Appendix A: X-ray/SDSS sub-samples

In Fig. A.1 we report the multicomponent simultaneous fit results of the 28 sources for which it was possible to well distinguish between different kinematic components in the forbidden doublet of singly ionised sulphur (Sect. 3.2). The flux ratios $R_{[SII]}$ derived for the entire set of 28 AGNs are reported in Table A.1; the doubly ionised oxygen ratios obtained for the sub-samples of AGNs defined in Sect. 3.1 and used to construct the histograms in Fig. 4 are reported in Table A.2.

Table A.1. Plasma diagnostics sub-samples.

SDSS name	ID-MJD-FIBER	z	Sample	$L_{[OIII]}$	$R_{[SII]}$	
(1)	(2)	(3)	(4)	(5)	(6)	(7)
J135317.8+332927	2117-54115-0351	0.0079	T13	39.88	1.06 ± 0.05	0.92 ± 0.14
J125725.2+272416	2241-54156-0195	0.0161	G11	39.49	1.23 ± 0.40	1.16 ± 0.28
J153457.2+233013	2163-53823-0058	0.0184	G11	39.19	1.38 ± 0.55	1.33 ± 0.15
J121049.6+392822	1995-53415-0205	0.0226	G11	39.94	0.96 ± 0.09	0.95 ± 0.15
J120429.6+201858	2608-54474-0555	0.0226	G11	41.17	0.99 ± 0.05	0.67 ± 0.10
J130125.2+291849	2011-53499-0492	0.0234	T13	40.66	1.16 ± 0.40	0.93 ± 0.45
J104451.7+063548	1000-52643-0080	0.0276	G11	40.98	1.00 ± 0.04	0.89 ± 0.09
J123651.1+453904	1372-53062-0412	0.0303	T13	40.67	1.34 ± 0.07	0.81 ± 0.08
J160515.8+174227	2200-53875-0423	0.0316	G11	40.41	1.13 ± 0.21	0.95 ± 0.31
J144921.5+631614	0609-52339-0531	0.0417	G11	41.17	0.97 ± 0.11	1.25 ± 0.10
J155855.7+024833	0595-52023-0179	0.0468	G11	40.85	1.26 ± 0.08	0.45 ± 0.08
J135602.6+182217	2756-54508-0198	0.0506	T13	41.11	1.24 ± 0.50	0.77 ± 0.50
J002920.3-001028	0391-51782-0155	0.0605	G11	40.84	0.98 ± 0.13	0.79 ± 0.08
J125558.7+291459	2011-53499-0244	0.0681	T13	41.13	1.12 ± 0.60	1.07 ± 0.60
J125830.1-015837	0338-51694-0480	0.0803	T13	41.18	1.14 ± 0.06	1.03 ± 0.10
J081444.2+363640	0892-52378-0579	0.0825	T13	40.80	1.33 ± 0.13	0.81 ± 0.22
J151141.2+051809	1832-54259-0119	0.0842	T13	41.71	1.12 ± 0.35	0.59 ± 0.18
J124415.2+165350	2601-54144-0282	0.0876	G11	40.84	1.34 ± 0.23	0.94 ± 0.18
J143602.5+330754	1841-53491-0584	0.0938	T13	41.36	1.15 ± 0.05	1.10 ± 0.36
J000703.6+155423	0751-52251-0577	0.1141	T13	41.94	1.16 ± 0.55	1.22 ± 0.60
J111847.0+075419	1617-53112-0469	0.1269	G11	41.48	0.77 ± 0.26	0.47 ± 0.11
J090935.5+105210	1739-53050-0421	0.1654	T13	42.33	1.04 ± 0.23	1.06 ± 0.20
J141602.1+360923	1643-53143-0153	0.1708	G11	41.50	1.32 ± 0.17	1.29 ± 0.25
J085331.0+175339	2281-53711-0179	0.1865	G11	42.56	1.11 ± 0.07	1.08 ± 0.12
J121249.8+065945	1624-53386-0056	0.2095	W12	40.89	1.16 ± 0.23	0.83 ± 0.15
J150407.5−024816	0922-52426-0127	0.2169	G11	42.02	1.24 ± 0.08	0.97 ± 0.05
J090036.8+205340	2282-53683-0103	0.2357	G11	42.57	1.33 ± 0.10	0.71 ± 0.13
J142314.2+505537	1045-52725-0072	0.2754	W12	42.89	1.13 ± 0.30	1.31 ± 0.26

Notes. Columns (1) and (2): names and MJD, plate and fibre numbers which identify the SDSS targets. Column (3): redshifts. Column (4): parent sample from which X-ray/SDSS targets have been selected (abbreviations: G11, Georgakakis et al. 2011; T13, Trichas et al. 2013; W12, Wu et al. 2012). Column (5): [O III]λ5007 total luminosity. Columns (6) and (7): NC and OC flux ratios between [S II]λ6716 and λ6731 lines.

Table A.2. Plasma diagnostics sub-samples – [O III] flux ratios.

SDSS name (1)	ID-MJD-FIBER (2)	z (3)	Sample (4)	$L_{[OIII]}$ (5)	$R_{[OIII]}$ (6)	(7)
J122546.7+123942	1615-53166-0388	0.0086	G11	40.95	127 ± 35	95 ± 23
J140040.5-015518	0915-52443-0437	0.0250	G11	41.07	102 ± 9	19 ± 2
J144012.7+024743	0536-52024-0575	0.0299	G11	41.16	71 ± 3	94 ± 15
J103408.5+600152	0560-52296-0520	0.0510	G11	42.44	284 ± 150	79 ± 5
J121839.4+470627	1451-53117-0190	0.0939	G11	42.16	245 ± 140	61 ± 4
J093952.7+355358	1594-52992-0417	0.1366	G11	42.34	95 ± 15	49 ± 2
*J090935.5+105210	1739-53050-0421	0.1654	T13	42.33	50 ± 4	44 ± 11
*J085331.0+175339	2281-53711-0179	0.1865	G11	42.56	63 ± 2	90 ± 11
J122548.8+333248	2015-53819-0251	0.0011	G11	38.92	52 ± 1	–
J134208.3+353915	2101-53858-0049	0.0036	G11	39.38	25 ± 1	–
J112613.7+564809	1309-52762-0263	0.0101	T13	39.44	76 ± 4	–
J081937.9+210651	1927-53321-0261	0.0185	G11	40.39	93 ± 6	–
J005329.9−084604	0657-52177-0458	0.0190	G11	40.79	115 ± 7	–
J104341.2+591653	0561-52295-0252	0.0285	T13	39.68	97 ± 4	–
J235951.7−092632	0650-52143-0461	0.0423	T13	41.09	54 ± 3	–
J080535.0+240950	1265-52705-0158	0.0597	G11	41.43	36 ± 2	–
J134427.5+560128	1321-52764-0624	0.0706	T13	41.12	187 ± 4	–
J122137.9+043026	2880-54509-0318	0.0947	G11	40.69	30 ± 2	–
*J120429.6+201858	2608-54474-0555	0.0226	G11	41.17	41 ± 3	41 ± 3
*J130125.2+291849	2011-53499-0492	0.0234	T13	40.67	61 ± 26	61 ± 26
J112301.3+470308	1441-53083-0560	0.0252	G11	40.95	44 ± 3	44 ± 3
J082443.2+295923	1207-52672-0500	0.0254	G11	41.19	89 ± 5	89 ± 5
J080359.2+234520	1265-52705-0271	0.0294	G11	41.08	58 ± 4	58 ± 4
J104930.9+225752	2481-54068-0247	0.0328	G11	41.25	59 ± 3	59 ± 3
J110929.3+284129	2213-53792-0223	0.0329	T13	40.87	32 ± 2	32 ± 3
J095914.7+125916	1744-53055-0385	0.0343	G11	41.47	86 ± 10	86 ± 10
J115704.8+524903	0882-52370-0430	0.0356	G11	41.26	84 ± 4	84 ± 4
J113549.0+565708	1311-52765-0262	0.0514	G11	41.69	75 ± 4	75 ± 4
J151640.2+001501	0312-51689-0471	0.0526	G11	41.04	9 ± 1	9 ± 1
J150754.3+010816	0540-51996-0253	0.0610	G11	41.53	51 ± 3	51 ± 3
J151106.4+054122	1833-54561-0404	0.0806	G11	41.61	49 ± 2	49 ± 2
J102147.8+131228	1746-53062-0513	0.0852	G11	41.09	18 ± 2	18 ± 2
J103014.4+431520	1429-52990-0131	0.0985	T13	41.65	48 ± 4	48 ± 4
*J000703.6+155423	0751-52251-0577	0.1141	T13	41.94	97 ± 45	97 ± 45
*J111847.0+075419	1617-53112-0469	0.1269	G11	41.49	25 ± 2	25 ± 2
J165939.7+183436	1567-53172-0113	0.1708	T13	42.28	69 ± 3	69 ± 3
J150719.9+002905	0310-51616-0565	0.1820	G11	42.63	55 ± 8	55 ± 8
J075820.9+392335	0544-52201-0464	0.2162	G11	42.66	89 ± 7	89 ± 7
*J090036.8+205340	2282-53683-0103	0.2357	G11	42.57	55 ± 2	55 ± 2
J083454.9+553421	5153-56577-0372	0.2415	G11	42.34	53 ± 5	53 ± 5
J131403.5+365438	2032-53815-0204	0.2967	T13	41.82	10 ± 1	10 ± 1
J134242.3+494439	1669-53433-0215	0.3473	T13	42.68	36 ± 3	36 ± 3
J153641.6+543505	0616-52374-0442	0.4471	G11	42.48	15 ± 4	15 ± 4
J080754.5+494627	1780-53090-0094	0.5753	W12	43.34	32 ± 3	32 ± 3

Notes. Columns (1) to (5): see Table A.2 for description. Columns (6) and (7): NC and OC doubly ionised oxygen flux ratios. Horizontal lines separate the sub-samples defined in Sect. 3.1: the first 8 rows are associated with sources with evidence of ionised outflows and well detected ($S/N > 10$) [O III]λ4363 lines. For these sources, both NC and OC flux ratios have been measured. The following 10 AGNs are not associated with ionised outflows and only NC flux ratios are reported. Finally, the last 26 rows are associated with AGNs with evidence of outflows but faint ($5 < S/N < 10$) [O III]λ4363 lines. For these sources, NC and OC flux ratios have been imposed to be equal (i.e. T_e(NC) = T_e(OC)). The sources marked with (*) are also present in the sample of 28 AGNs with measured [S II] flux ratios.

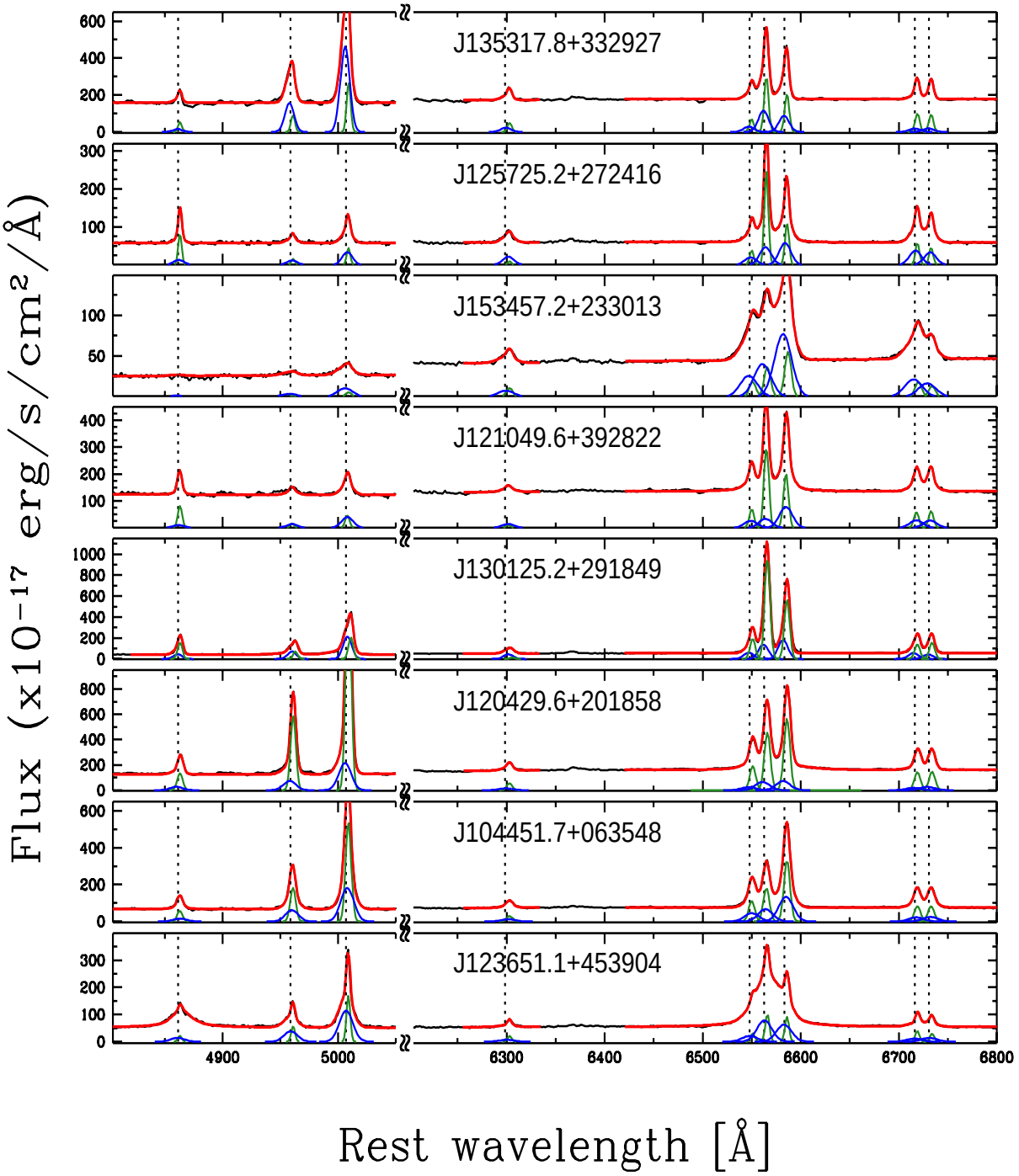

Fig. A.1. Rest-frame optical spectra of 8 out 28 AGNs for which we derive density-sensitive flux ratios. For each object, we show the spectrum (black curve) and the best-fit models (red curves) obtained from multicomponent simultaneous fit in the regions around the Hβ and the Hα emission. The dashed vertical lines mark the location of Hβ, [O III] doublet, [O I], Hα, [N II] and [S II] doublets. Best-fit NC and BC profiles are shown with green curves; blue curves show OC emission.

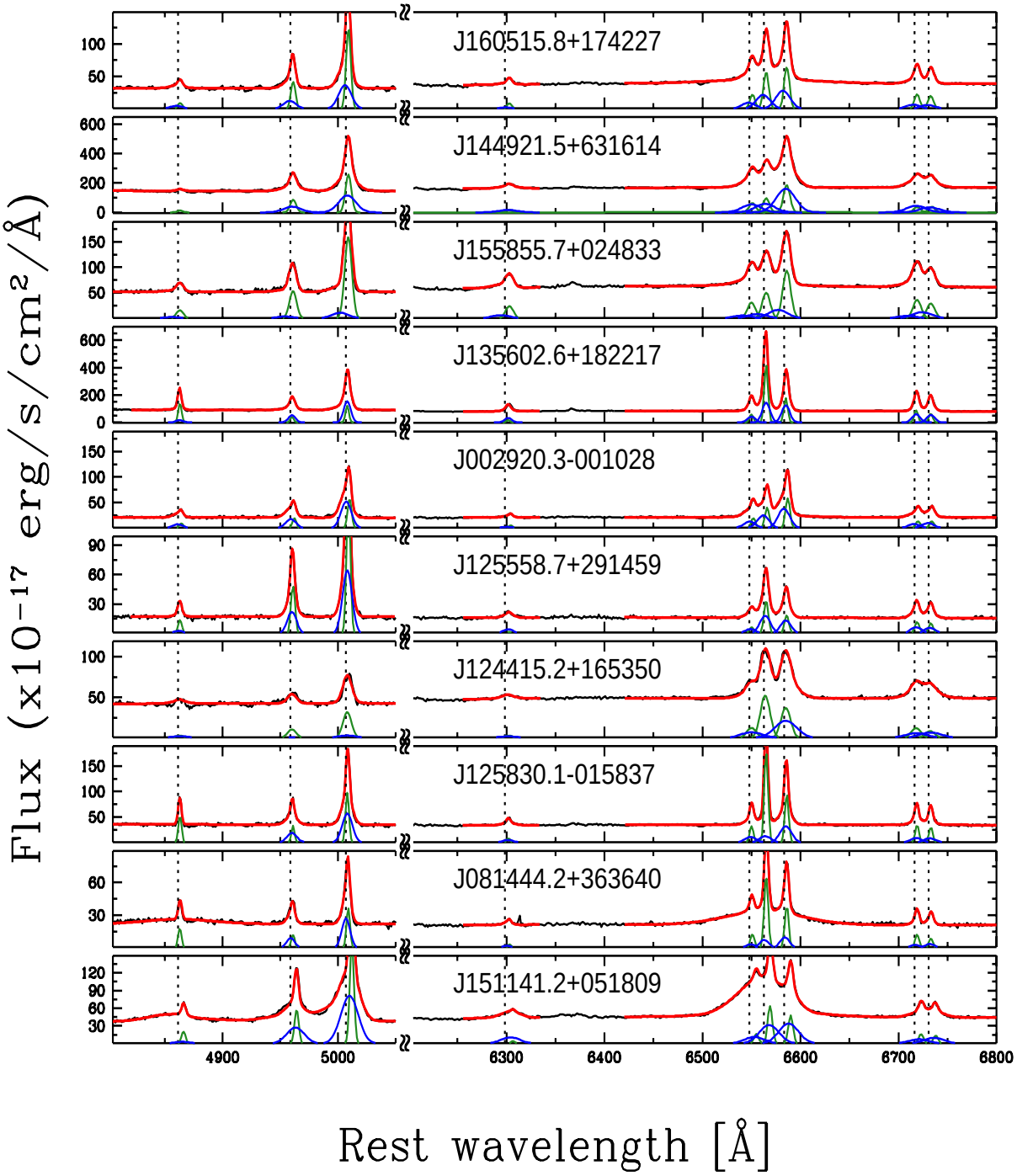

Fig. A.1. continued.

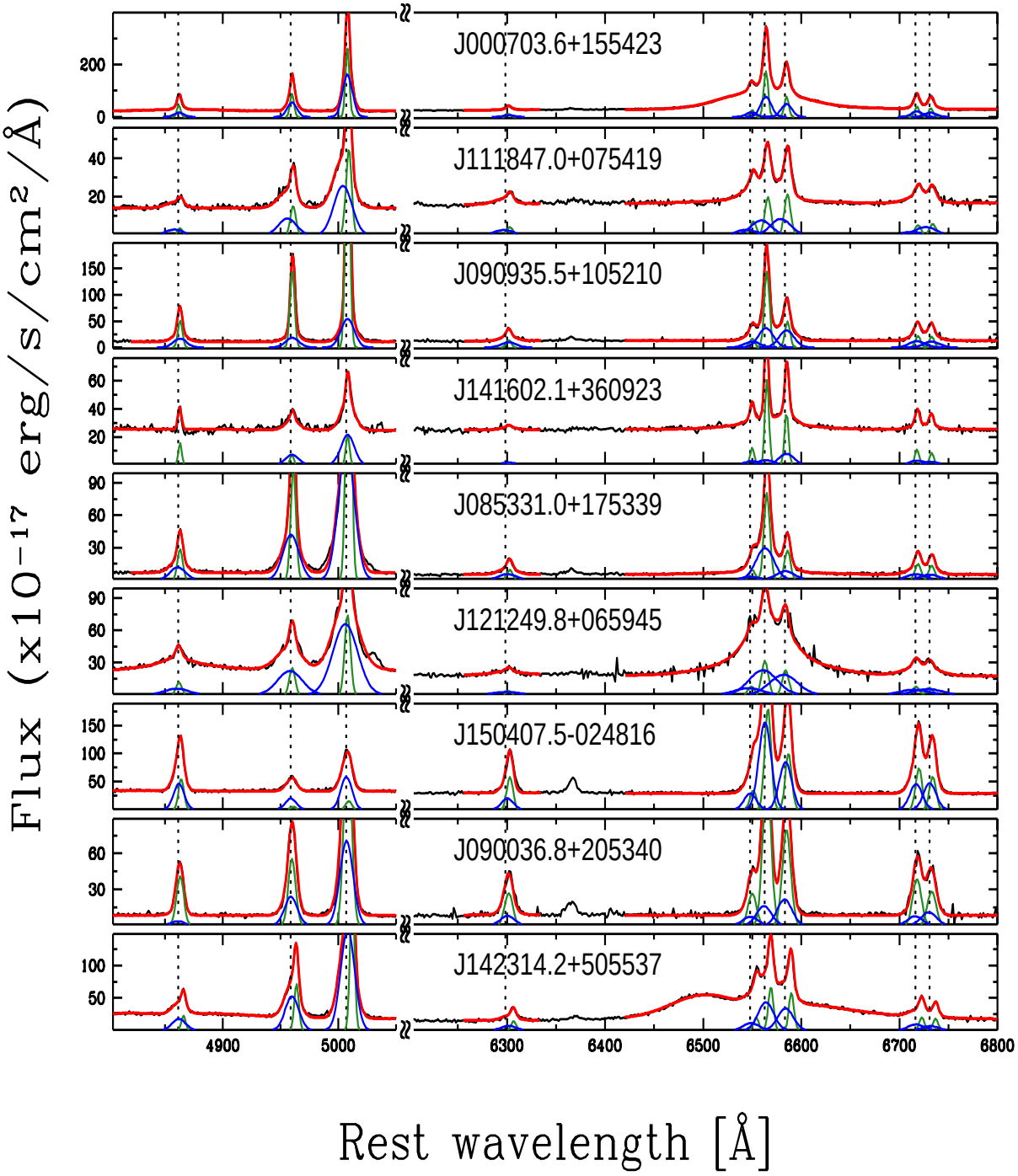

Fig. A.1. continued.